Icarus 285 (2017) 155–168

Contents lists available at ScienceDirect

Icarus

journal homepage: www.elsevier.com/locate/icarus

Geochemistry, mineralogy, and petrology of boninitic and komatiitic rocks on the mercurian surface: Insights into the mercurian mantle

Kathleen E. Vander Kaaden[a,b,c,*], Francis M. McCubbin[a,c], Larry R. Nittler[d], Patrick N. Peplowski[e], Shoshana Z. Weider[d], Elizabeth A. Frank[d], Timothy J. McCoy[f]

[a] Institute of Meteoritics, Department of Earth & Planetary Sciences, University of New Mexico, Albuquerque, NM 87131, USA
[b] Lunar and Planetary Institute, 3600 Bay Area Boulevard, Houston, TX 77058, USA
[c] NASA Johnson Space Center, Mailcode XI2, 2101 NASA Parkway, Houston, TX 77058, USA
[d] Department of Terrestrial Magnetism, Carnegie Institution of Washington, DC 20015, USA
[e] The Johns Hopkins University Applied Physics Laboratory, Laurel, MD 20723, USA
[f] Department of Mineral Sciences, National Museum of Natural History, 10th and Constitution Aves. NW, Smithsonian Institution, Washington, DC 20560, USA

ARTICLE INFO

Article history:
Received 22 June 2016
Revised 1 November 2016
Accepted 30 November 2016
Available online 8 December 2016

Keywords:
Mercury
Petrologic classification
IUGS
Boninites
Komatiites

ABSTRACT

Orbital data from the MESSENGER mission to Mercury have facilitated a new view of the planet's structure, chemical makeup, and diverse surface, and have confirmed Mercury's status as a geochemical endmember among the terrestrial planets. In this work, the most recent results from MESSENGER's X-Ray Spectrometer, Gamma-Ray Spectrometer, and Neutron Spectrometer have been used to identify nine distinct geochemical regions on Mercury. Using a variation on the classical CIPW normative mineralogy calculation, elemental composition data is used to constrain the potential mineralogy of Mercury's surface; the calculated silicate mineralogy is dominated by plagioclase, pyroxene (both orthopyroxene and clinopyroxene), and olivine, with lesser amounts of quartz. The range in surface compositions indicate that the rocks on the surface of Mercury are diverse and vary from komatiitic to boninitic. The high abundance of alkalis on Mercury's surface results in several of the nine regions being classified as alkali-rich komatiites and/or boninites. In addition, Mercury's surface terranes span a wide range of SiO_2 values that encompass crustal compositions that are more silica-rich than geochemical terranes on the Moon, Mars, and Vesta, but the range is similar to that of Earth. Although the composition of Mercury's surface appears to be chemically evolved, the high SiO_2 content is a primitive feature and a direct result of the planet's low oxygen fugacity.

1. Introduction

Prior to the return of data from the MErcury Surface, Space ENvironment, GEochemistry, and Ranging (MESSENGER) mission (Solomon et al., 2001), data relating to Mercury were scarce, resulting in much information about the planet having to be inferred. During the Mariner 10 flybys in 1974 and 1975, ~45 % of the planet was imaged, a magnetic field was detected, H, He, and O in the exosphere were measured, and other physical characteristics of the planet were determined (Broadfoot et al., 1974,1976; Chase et al., 1974; Murray, 1975; Ness et al., 1974, 1975). NASA's MESSENGER mission (Solomon et al., 2001), however, has provided the first in-depth study of the innermost planet. The onboard X-Ray Spectrometer (XRS) and Gamma-Ray and Neutron Spectrometer (GRNS) were used to obtain the first chemical analyses of Mercury's surface (Evans et al., 2012, 2015; Nittler et al., 2011; Peplowski et al., 2012a, 2012b, 2014, 2015a, 2015b, 2016; Weider et al., 2012, 2014, 2015, 2016). With XRS data, the abundance of major rock-forming elements in the top ~100 μm of the surface were quantified, including fluorescent lines from Mg, Al, Si, S, Ca, Ti, and Fe (Nittler et al., 2011; Weider et al., 2012, 2014, 2015, 2016). In addition, the concentration of several elements (e.g., H, C, O, Na, Mg, Al, Si, Cl, Ca, Ti, and Fe) in the top ~10–40 cm of the surface were estimated from the Gamma-Ray Spectrometer (GRS) component of the GRNS (Evans et al., 2012, 2015; Peplowski et al., 2011, 2012a, 2012b, 2014, 2015a, 2015b, 2016). Data obtained from the Neutron Spectrometer (NS) allowed differences in the emission of epithermal, thermal, and fast neutrons across Mercury's surface to be measured. These data, for example were used to map the H content at Mercury's polar regions (and to provide complementary compositional information to XRS and GRS) by mapping differences in the flux

* Corresponding author at: Institute of Meteoritics, Department of Earth & Planetary Sciences, University of New Mexico, Albuquerque, NM 87131, USA.
E-mail addresses: kvander@unm.edu, kathleen.e.vanderkaaden@nasa.gov (K. E. Vander Kaaden).

http://dx.doi.org/10.1016/j.icarus.2016.11.041
0019-1035/

of neutrons, of varying energy, that are emitted due to interactions of cosmic rays with Mercury's surface (Lawrence et al., 2010, 2013, 2017). With the recent availability of data from the MESSENGER mission, it is our aim to conduct a systematic study to understand the mineralogy and petrology of the surface of Mercury and to provide an improved understanding of the geochemistry, mineralogy, and petrology of Mercury's mantle.

Given its close proximity to the Sun, Mercury was expected to be depleted in volatile elements (Albarède, 2009). Additionally, ultraviolet-visible light measurements of Mercury's surface from ground-based telescopes did not yield a definitive 1-μm absorption feature (McCord and Clark, 1979; Vilas, 1988) diagnostic of crystal field transitions in Fe^{2+} in the crystal structures of ferromagnesian silicates (Burns, 1993). This observation led to inferences that, like the lunar highlands, the surface of Mercury was low in FeO (Blewett et al., 1997, 2009; McClintock et al., 2008; McCord and Clark, 1979; Riner et al., 2010; Robinson and Lucey, 1997; Robinson et al., 2008; Vilas, 1988), but the abundance could not be constrained with a high level of certainty. Furthermore, Mercury – with its high density of craters and abundant smooth plains (similar in appearance to the lunar maria) – was frequently compared with the Moon (Blewett et al., 2002; Taylor and Scott, 2004). It was also thought that Mercury's reflectance spectra were similar to those of the plagioclase-dominated lunar highlands (e.g., Blewett et al., 2002; Hapke, 1977), although mid-infrared telescopic thermal emission data suggested it was more sodic and variable in nature (Sprague and Roush, 1998). By analogy to the Moon, formation of a plagioclase floatation crust from a magma ocean event on Mercury has also been suggested (Brown and Elkins-Tanton, 2009; Riner et al., 2009; Taylor, 2009). However, estimates of low FeO abundances on Mercury as observed from MESSENGER could inhibit plagioclase floatation within a mercurian magma ocean (Vander Kaaden and McCubbin, 2015). The resolution and coverage of Mariner 10 mapping of Mercury's surface was inadequate to determine whether Mercury's bulk surface was a primary crust (subsequently modified substantially by the late heavy bombardment) or a secondary crust produced by volcanism (Taylor and McLennan, 2009).

Results from the geochemistry payload onboard MESSENGER have been used to identify numerous previously unknown geochemical features on Mercury's surface (e.g., Peplowski et al., 2015b; Weider et al., 2015). Furthermore, the data have revealed several surprising characteristics about the planet's surface, including elevated S abundances (up to 4 wt%) and low Fe abundances (less than 2 wt%) (Evans et al., 2012; Nittler et al., 2011; Weider et al., 2014). Such S and Fe concentrations have also been used to infer Mercury's highly reduced nature. It has been estimated that Mercury's interior is between 2.6 and 7.3 $\log_{10}$ units below the Iron-Wüstite (IW) buffer (McCubbin et al., 2012; Zolotov et al., 2013), which is lower than any other terrestrial planet in the Solar System (Herd, 2008; Sharp et al., 2013; Wadhwa, 2008). This highly reducing nature has important consequences for the thermal and magmatic evolution of Mercury, its surface mineralogy and geochemistry, as well as the petrogenesis of mercurian magmas (Brown and Elkins-Tanton, 2009; Charlier et al., 2013; McCubbin et al., 2012; Namur et al., 2016; Nittler et al., 2011; Stockstill-Cahill et al., 2012; Vander Kaaden and McCubbin, 2015, 2016). Although previous work has examined the potential mineralogy associated with various regions on Mercury (Charlier et al., 2013; Namur et al., 2016; Stockstill-Cahill et al., 2012; Vander Kaaden and McCubbin, 2016), the most up-to-date geochemical results from MESSENGER have not yet been used to understand the mineralogy and petrology across the surface of the planet.

Several geochemical regions have previously been identified on the surface of Mercury on the basis of their composition, as measured by the XRS and GRS (Peplowski et al., 2015b; Weider et al., 2015). The oxide compositions of these geochemical terranes – calculated according to the methods of Vander Kaaden and McCubbin (2016) – indicate a variable Si abundance across Mercury's surface and suggest that MESSENGER's geochemical results pertain to a diverse set of rocks and minerals. To date, it has been suggested that Mercury's surface compositions are akin to terrestrial komatiites, because of their Mg/Si and Al/Si ratios (Nittler et al., 2011; Weider et al., 2015), and to terrestrial boninites, given the high (calculated) SiO_2 abundances of some regions (e.g., Vander Kaaden and McCubbin, 2016). However, given the newest results from MESSENGER, it is possible that this diversity in geochemistry, mineralogy, and petrology, is even greater than previously suggested. In the present study, we compare the geochemistry of nine distinct geochemical terranes identified by MESSENGER to gain a deeper understanding of the lithologic diversity on the mercurian surface and its implications for mineralogy of the surface and mantle of Mercury.

2. Methods

We used XRS (Nittler et al., 2011; Weider et al., 2012, 2014, 2016) and GRS (Peplowski et al., 2012a, 2014) analyses to determine the average compositions for nine identified geochemical regions (see Tables 1 and 2). Although C has recently been identified on the surface of Mercury (Murchie et al., 2015; Peplowski et al., 2015a, 2016), the source of this C is still debated (Bruck et al., 2015; Murchie et al., 2015; Peplowski et al., 2015a, 2016; Vander Kaaden and McCubbin 2016); therefore, we have not included C in our calculations. The elemental data from the XRS that we used, which incorporated data from the low-altitude campaign at the end of the MESSENGER mission (Weider et al., 2016), included Mg/Si, Ca/Si, Al/Si, Fe/Si, and S/Si ratios. Due to the highly elliptical polar orbit of MESSENGER, the spatial resolutions of XRS and GRNS measurements varied across the planet's surface, with higher resolution obtained at northern latitudes. XRS resolution varied from $<$100 km at mid-northern latitudes to $>$3000 km over the south pole. Spatial coverage from the different geochemical instruments also varied. Whereas XRS maps of Mg/Si and Al/Si cover the globe, XRS maps of S/Si, Ca/Si and Fe/Si ratios are all more limited in extent (Weider et al., 2016). Therefore, the geochemical regions discussed here are largely defined on the basis of the Mg/Si, Al/Si, and neutron maps, which have the greatest spatially resolved northern hemisphere coverage, although at least some heavier element data are available for all geochemical regions of interest. Because the regions are larger than the measurement resolution, we calculated area-weighted averages for each region to avoid over-interpretation of any single pixel.

The spatial resolution of the GRS measurements varies as ~1.5x the spacecraft altitude. For GRS K measurements, abundances were mapped in pixels whose sizes were varied as a function of latitude, whereas Na measurements were reported for latitude bands. In both cases, the pixels/bands were sized to achieve a useful statistical precision for each measurement, and we note that their spatial extents were comparable to, or larger than, the intrinsic spatial resolution of the GRS data. All other GRS element measurements were provided as "northern hemisphere averages". For these measurements, low-altitude ($<$2000 km) data were used, during which time the sub-spacecraft latitude ranged from approximately −20° to 90°, with spatial coverage being heavily biased to latitudes $>$25°

2.1. Identification of distinct geochemical regions

To investigate the potential mineralogical and petrologic diversity of Mercury, we have focused our investigation on nine distinct geochemical regions. These regions are shown on a map of Mercury in Fig. 1 and include (i) the high-Mg region (HMR); (ii) a sub-region of the HMR with the planet's highest Ca and S contents (HMR-CaS); (iii) a subset of the northern volcanic plains (NP)

Table 1
Average compositions (wt%) for nine distinct geochemical regions on Mercury using only reported values for Ti, Mn, and Cr. Standard error is given parenthetically. The reader is referred to Section 2.1. for details regarding calculations of these compositions.

	HMR	HMR-CaS	NP-HMg	NP-LMg	RB	PD	HAl	CB	IT
SiO_2	51.81 (7.04)	50.50 (5.95)	54.89 (7.49)	60.70 (7.43)	52.40 (4.17)	53.08 (1.45)	55.42 (4.23)	58.86 (4.75)	55.89 (8.05)
MgO	24.15 (2.86)	25.14 (2.32)	20.28 (3.90)	12.50 (2.84)	23.42 (2.12)	21.81 (0.45)	16.50 (1.47)	13.05 (2.28)	17.94 (4.62)
CaO	7.00 (1.70)	7.76 (1.35)	5.58 (1.20)	5.43 (1.23)	6.84 (0.63)	7.46 (0.14)	5.73 (1.59)	5.70 (0.63)	5.74 (0.93)
Al_2O_3	10.05 (1.36)	9.27 (1.82)	12.57 (1.51)	12.16 (2.40)	10.45 (0.88)	11.72 (0.47)	16.78 (0.57)	16.59 (0.97)	14.06 (1.80)
K_2O	0.16 (0.03)	0.16 (0.03)	0.24 (0.04)	0.18 (0.04)	0.16 (0.03)	0.16 (0.03)	0.16 (0.03)	0.09 (0.02)	0.11 (0.02)
Na_2O	3.51 (0.01)	3.51 (0.01)	3.51 (0.01)	6.47 (0.04)	3.51 (0.01)	3.51 (0.01)	3.51 (0.01)	3.51 (0.01)	3.51 (0.01)
FeO	1.99 (0.51)	2.19 (0.31)	2.02 (0.31)	1.62 (0.47)	1.94 (0.31)	1.98 (0.31)	0.97 (0.31)	0.99 (0.21)	1.84 (0.34)
TiO_2	0.00	0.00	0.00	0.00	0.00	0.00	0.00	0.46 (0.16)	0.00
CrO	0.00	0.00	0.00	0.00	0.00	0.00	0.00	0.00	0.00
MnO	0.00	0.00	0.00	0.00	0.00	0.00	0.00	0.00	0.00
S	2.67 (0.60)	2.96 (0.29)	1.80 (0.57)	1.88 (0.49)	2.57 (0.24)	0.57 (0.07)	1.88 (0.07)	1.52 (0.50)	1.81 (0.37)
-O=S	1.33	1.48	0.90	0.94	1.28	0.28	0.94	0.76	0.90
Total	100.00	100.00	100.00	100.00	100.00	100.00	100.00	100.00	100.00
Wt% Si	24.22 (4.66)	23.61 (3.75)	25.66 (4.82)	28.37 (4.72)	24.50 (2.67)	24.81 (0.94)	25.90 (2.85)	27.51 (3.09)	26.13 (5.04)
Total Alkalis	3.66 (0.04)	3.66 (0.04)	3.75(0.05)	6.65 (0.08)	3.66 (0.04)	3.66 (0.04)	3.66 (0.04)	3.60 (0.04)	3.62 (0.03)

Table 2
Average compositions (wt%) for the nine geochemical regions. These compositions were calculated in the same way as those shown in Table 1, but where the detection limits of Ti, Mn, and Cr (Nittler et al., 2011; Weider et al., 2015) were used as an *upper limit* (if abundance estimates for these elements were not available).

	HMR	HMR-CaS	NP-HMg	NP-LMg	RB	PD	HAl	CB	IT
SiO_2	50.52 (7.04)	49.27 (5.95)	53.44 (7.49)	58.87 (7.43)	51.08 (4.17)	51.72 (1.45)	53.94 (4.23)	58.00 (4.75)	54.38 (8.05)
MgO	23.54 (2.86)	24.52 (2.32)	19.75 (3.90)	12.13 (2.84)	22.82 (2.12)	21.25 (0.45)	16.06 (1.47)	12.86 (2.28)	17.46 (4.62)
CaO	6.82 (1.70)	7.57 (1.35)	5.43 (1.20)	5.27 (1.23)	6.66 (0.63)	7.27 (0.14)	5.58 (1.59)	5.62 (0.63)	5.59 (0.93)
Al_2O_3	9.80 (1.36)	9.04 (1.82)	12.24 (1.51)	11.79 (2.40)	10.19 (0.88)	11.42 (0.47)	16.34 (0.57)	16.35 (0.97)	13.68 (1.80)
K_2O	0.16 (0.03)	0.16 (0.03)	0.24 (0.04)	0.18 (0.04)	0.16 (0.03)	0.16 (0.03)	0.16 (0.03)	0.09 (0.02)	0.11 (0.02)
Na_2O	3.51 (0.01)	3.51 (0.01)	3.51 (0.01)	6.47 (0.04)	3.51 (0.01)	3.51 (0.01)	3.51 (0.01)	3.51 (0.01)	3.51 (0.01)
FeO	1.94 (0.51)	2.14 (0.31)	1.97 (0.31)	1.57 (0.47)	1.89 (0.31)	1.93 (0.31)	0.94 (0.31)	0.97 (0.21)	1.79 (0.34)
TiO_2	*1.18*	*1.15*	*1.25*	*1.38*	*1.20*	*1.21*	*1.26*	0.45 (0.16)	*1.27*
CrO	*0.62*	*0.60*	*0.65*	*0.72*	*0.62*	*0.63*	*0.66*	*0.71*	*0.66*
MnO	*0.61*	*0.59*	*0.65*	*0.71*	*0.62*	*0.62*	*0.65*	*0.70*	*0.66*
S	2.60 (0.60)	2.89 (0.29)	1.75 (0.57)	1.82 (0.49)	2.50 (0.24)	0.56 (0.07)	1.83 (0.07)	1.50 (0.50)	1.76 (0.37)
-O=S	1.30	1.44	0.87	0.91	1.25	0.28	0.91	0.75	0.88
Total	100.00	100.00	100.00	100.00	100.00	100.00	100.00	100.00	100.00
Wt% Si	23.61 (4.66)	23.03 (3.75)	24.98 (4.82)	27.52 (4.72)	23.88 (2.67)	24.18 (0.94)	25.21 (2.85)	27.11 (3.09)	25.42 (5.04)
Total Alkalis	3.66 (0.04)	3.66 (0.04)	3.75 (0.05)	6.65 (0.08)	3.66 (0.04)	3.66 (0.04)	3.66 (0.04)	3.60 (0.04)	3.62 (0.03)

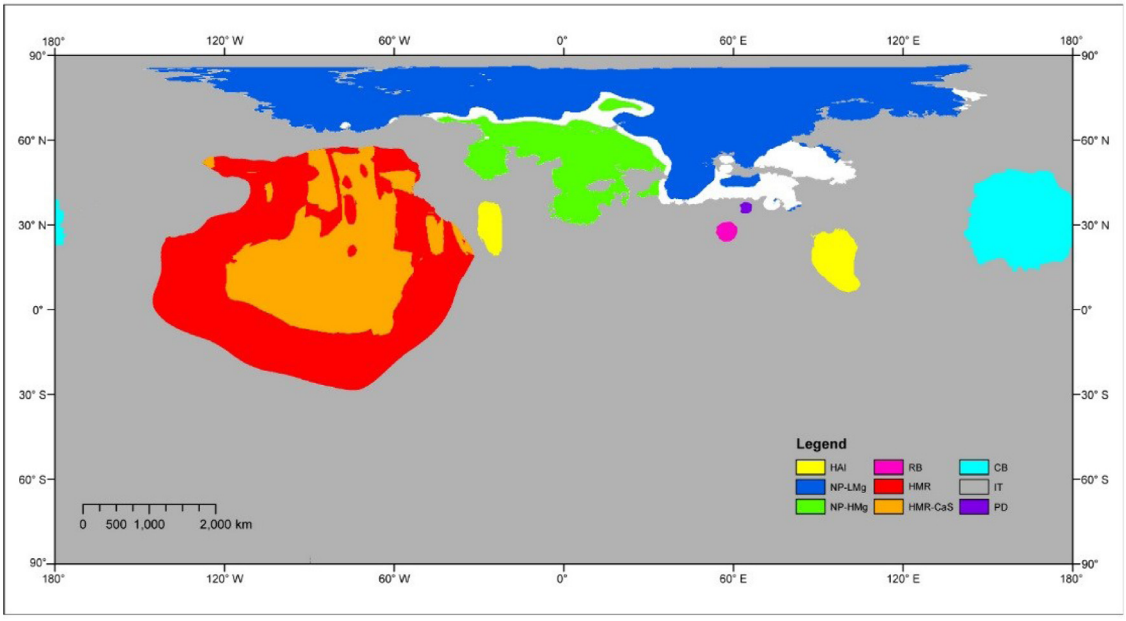

Fig. 1. Map of Mercury showing the nine geochemical regions defined on the basis of MESSENGER X-Ray Spectrometer (XRS) data. White areas indicate regions not considered in our calculations. The reader is referred to Section 2.1 for an explanation of each regions' acronym.

with relatively high Mg content (NP-HMg), distinguished by low-fast neutrons (Lawrence et al., 2017); (iv) a subset of the NP with relatively low Mg content (NP-LMg); (v) the Rachmaninoff basin (RB); (vi) the planet's largest pyroclastic deposit, located northeast of the Rachmaninoff basin (PD); (vii) the high-Al regions southwest and southeast of the NP (HAl); (viii) the smooth plains within the Caloris basin (CB); and (ix) the intermediate terrane (IT), made up of intercrater plains, highly-cratered terrain, and the southern hemisphere. The boundary of the CB plains and the outer NP boundary were based on the map of smooth plains by Denevi et al., (2013); all other region boundaries were defined based on the XRS and NS maps.

We defined the NP-HMg region (see Fig. 1) as those pixels within the NP with Mg/Si $\sim>0.4$ that is also confined to the center longitude regions, i.e. between $\pm60°$, which is consistent with the "low fast neutron" region described by Lawrence et al., (2017). Furthermore, we defined the NP-LMg region (Fig. 1) as the NP pixels with Mg/Si < 0.35 (it therefore includes most of the NP). Although only one Al-rich terrane (at $-25°$E, $+30°$N), has previously been identified (Weider et al., 2015), our updated geochemical maps reveal the presence of a second area with a similar chemistry (at $+96°$E, $+20°$N). Therefore, we include both areas in our HAl region. The HMR, RB, PD, and CB regions have been defined in previous publications (Blair et al., 2013; Oberst et al., 2010;Weider et al., 2015, 2016). We defined the IT as the remainder of the planet (i.e., not included in any of the other eight regions), which includes the southern hemisphere, intercrater plains, and heavily-cratered terrain. The elemental ratios and standard errors used to define each geochemical region are given in Table S1.

Although the abundances of Ti, Mn, and Cr have been reported for some XRS measurements (Nittler et al., 2011; Weider et al., 2014, 2015), they have not yet been systematically mapped and are not available for most of our defined units. In our work we have calculated two average compositions for each geochemical region. For the first calculated composition of each geochemical region (Table 1), we only considered values of Ti, Mn, and Cr for regions where they are reported. For the second set of calculated compositions (Table 2), we used the reported XRS detection limits for Ti, Mn, and Cr (Nittler et al., 2011; Weider et al., 2014, 2015) as the concentrations of these elements when abundances were below detection.

We also derived alkali abundances for these regions from GRS measurements. Low GRS counting statistics did not permit mapping of Na abundances, but Na/Si was found to vary with latitude (Peplowski et al., 2014), with an inferred equatorial Na abundance of 2.6 wt% and a greater value of 4.8 wt% at high northern latitudes. Here, we assign the higher value to the NP-LMg region and the lower value to all the other regions. In terms of K, we used the previously published K map, derived from GRS measurements (Peplowski et al., 2012a), to assign a suitable K_2O abundance to each of our geochemical regions. Specifically, we used the "All 2012″ of Peplowski et al. (2012a, 2012b) to assign the K abundance for the HMR, HMR-CaS, RB, HAl, and PD regions, their "CB" value for our CB region, and their "ICP/HCT/SP" value for the K abundance of our IT region. We have also produced updated K abundances for the NP-HMg and NP-LMg (0.2 and 0.15 wt%, respectively), refined from Peplowski et al., (2012a), where we discriminate between the NP-HMg and NP-LMg, which has not been done prior to this work.

To determine the composition of each distinct geochemical region, we employed a similar approach to that of Vander Kaaden and McCubbin (2016). First, we assigned the valence of each element (i.e., Si^{4+}, Ti^{4+}, Al^{3+}, Cr^{2+}, Fe^{2+}, Mn^{2+}, Mg^{2+}, Ca^{2+}, Na^{+}, K^{+}, S^{2-}). We then calculated a corresponding abundance of O^{2-}, so that the resulting composition for each specific region was charge-balanced. Assuming no major constituent elements have been excluded, the resulting sum of oxides/sulfides should thus be $\sim$100 wt%. In the final step of our procedure, we normalized each region's composition to 100 wt%, which maintains the measured element/Si ratios given in Table S1. From these calculations, we found that the resulting O/Si values ranged from 1.58–1.91.

The standard error for each oxide is reported in Tables 1 and 2. We derived these errors by taking the standard error from XRS (element—to—Si ratios) and GRS (elemental) measurements, calculating the standard error for the element of interest (i.e., Mg, Ca, S, Al, K, Na, Fe, Ti), and converting this value to the standard error for the oxide or sulfide of interest (i.e., MgO, CaO, S^{2-}, Al_2O_3, K_2O, Na_2O, FeO, TiO_2). When we used the detection limits for Ti, Mn, and Cr, no standard errors are reported. Furthermore, due to the dependence on Si in each calculated composition, the error on SiO_2 is the sum of the errors for all oxides analyzed by XRS. These computations result in $\sim$4–19% error on Si, which is still within, or less than, the range of error reported for Si by GRS (i.e. $<$15% across the northern hemisphere, Peplowski et al., 2012a). In addition, the difference between Tables 1 and 2 is the inclusion of detection limits for Cr, Mn, and Ti, so the standard error on the oxides are the same in both tables.

2.2. Normative mineralogy calculations & petrologic classification

Although each geochemical region may not represent a single rock type or a specific set of minerals that can be easily deduced by bulk normative mineralogical calculations, the results of our calculations are useful for studying the geochemistry, mineralogy, and petrology of Mercury's surface (especially from the standpoint of comparative planetary geochemistry). Consequently, we calculated a CIPW norm (Cross et al., 1903) and we petrologically classified – according to the International Union of Geological Sciences (IUGS) classification protocols (Le Bas, 2000 and references therein; Le et al., 2002) – each of the nine geochemical regions. We note, however, that our classifications are based solely on the chemical composition for each unit and they should not be used, *a priori*, to infer geologic processes or settings.

The high S content of the mercurian compositions means that CIPW normative mineralogy calculations cannot be conducted in the conventional manner because there is not enough Fe to accommodate S in most cases. Instead, we first calculated the sulfides that would be present in each composition by using the experimentally calculated sulfide-melt partition coefficients of Vander Kaaden and McCubbin (2016). With this method, which is based on experiments conducted at Mercury-relevant geochemical conditions, FeS, CrS, TiS_2, and MnS are initially produced. If any S remains after the Fe, Cr, Ti, and Mn have been consumed then MgS and CaS are produced – with a sulfide–melt Ca–Mg exchange coefficient of 1.97 (Vander Kaaden and McCubbin, 2016) – until all the S is consumed. At the point when all S has been consumed by sulfides, we renormalized the remaining composition to 100% and thus produced a S-free composition. We then calculated – according to the methodology of Johannsen (1931) – the normative mineralogy of each geochemical region from this S-free composition. We did, however, make a modification to this classical calculation for the treatment of MnO. Typically, it is assumed that MnO acts like FeO and it is thus included in the calculation of an ilmenite component. However, given the highly reducing nature of Mercury (McCubbin et al., 2012; Zolotov et al., 2013), as well as the low amount of Fe and Ti on the surface (Evans et al., 2012; Nittler et al., 2011; Weider et al., 2012, 2014, 2015), it is unlikely that ilmenite is present at concentrations sufficient to host the concentrations of Mn assigned to Mercury. In our approach, therefore, we put any MnO that was left after making MnS into a manganosite (MnO) component (although this component is probably consumed by olivine and/or pyroxene in the actual surface compositions).

3. Results

3.1. Major-element compositions

From our calculated compositions (Tables 1 and 2) for the nine geochemical regions (considering both sets of Cr, Mn, and Ti values), we determine a total range of ~5.3 wt% Si across Mercury's surface. This corresponds to a full range (Δ) of ~11.4 wt% SiO_2 across the nine geochemical regions. After our normalization step (and accounting for both sets of Cr, Mn, and Ti values), we find that SiO_2, MgO, and Al_2O_3 are the oxides with the largest range across the planet's surface ($\Delta = 11.43$, $\Delta = 13.01$, and $\Delta = 7.74$ wt%, respectively). Our results indicate that sulfides and all other oxides vary by $\Delta < 3$ wt%.

3.2. Normative mineralogy

The results of our normative mineralogy calculations are given in Fig. 2, Fig. S1, Table S2 and Table S3. We find that all of our geochemical regions are hypersthene normative, with the exception of the HMR-CaS, which is slightly nepheline normative with ~0.7–3.1 wt% nepheline. However, given the uncertainty on the oxides listed in Tables 1 and 2, we do not place too much confidence on this result or other results of similar magnitude. In terms of silica saturation, CB is quartz-normative, whereas the rest of the geochemical regions are consistently olivine-normative. Depending on the amount of Cr, Mn, and Ti present, the HAl region appears to be either olivine-normative (containing ~7 wt% olivine) or quartz-normative (containing ~0.4 wt% quartz); however, given the ~11% error on SiO_2, this normative abundance of quartz is extremely low and cannot be resolved with confidence.

Our calculations also indicate that the major minerals present on Mercury's surface – prior to, or in the absence of, any secondary degassing processes – include plagioclase, olivine, orthopyroxene, clinopyroxene, and quartz. Albitic plagioclase ($NaAlSi_3O_8$) consistently dominates all regions (32.42–58.35 wt%), which reflects the alkali-rich nature of Mercury. Olivine (0–34.59 wt%) is much more dominant in the HMR, HMR-CaS, RB, and PD regions (representing ≥~30 wt% of the normative calculations) than in the NP, HAl, and IT regions (where it only makes up ≤~16 wt% of the bulk compositions). As stated above, we find that the CB is consistently olivine-free. Our results show that orthopyroxene is the dominant pyroxene phase in the NP-HMg, HAl, CB, and IT regions (i.e., hypersthene 23.51–37.13 wt%), whereas clinopyroxene dominates in the HMR, HMR-CaS, RB, and PD (i.e., diopside 16.04–22.43 wt%), and the NP-LMg has almost equal proportions of orthopyroxene and clinopyroxene. Although we find the presence of quartz only in the CB (≤8 wt%), it is the dominant minor mineral in that region.

Our normative mineralogy results (Fig. 2) also illustrate the similarity of the HMR and HMR-CaS, where the main difference between the two is the abundance of orthopyroxene. Furthermore, the two NP regions have similar mineralogy, with the NP-HMg containing ~10 wt% more olivine, and ~10 wt% less clinopyroxene, than the NP-LMg. The mineralogy of the RB and PD regions are also similar, although PD has fewer sulfides (1.56 wt% vs. 5.42 wt%) and less orthopyroxene (6.09 wt% vs. 11.45 wt%), as well as higher abundances of plagioclase (45.45 wt% vs. 41.99 wt%) and olivine (29.37 wt% vs. 24.17 wt%). Interestingly, the HAl and CB regions have extremely similar normative mineralogy. The only significant differences are in terms of orthopyroxene (~7 wt% higher in the HAl) and quartz (~8 wt% greater in the CB). It is also important to note that it is impossible to distinguish between a homogenous surface dominated by orthopyroxene and a heterogeneous surface with orthopyroxene and sub-equal amounts of olivine and silica.

Sulfides are the next-most abundant minerals in our CIPW normative calculations and we first consider them as a single, multi-component phase that makes up ~1.6–6.5 wt% of the normative mineralogy (Figs. 2 and S1). We find that sulfides are the most abundant in the HMR-CaS, which is consistent with this region containing the highest S abundances on the planet. The

HMR and RB both contain >5 wt% sulfides, whereas the NP, IT, and HAl regions contain ~4 wt% sulfides. The PD, which exhibits amongst the lowest S/Si ratio on the planet (Weider et al., 2016), also contains the least sulfides according to our calculations. We have also examined the individual sulfide components in each geochemical region (see Figs. 3 and S2). When we use only the measured values of Cr, Mn, and Ti in our calculations, we find that TiS_2 is present only in the CB (~0.6 wt%), and that MgS and CaS are present in all regions with the exception of the PD. Furthermore, MgS is consistently more abundant than CaS (a direct result of the sulfide–melt Ca–Mg exchange coefficient we used and the fact that the abundance of Mg > Ca in all regions). Including the results from Fig. S2, which takes into account the detection limits of Cr, Mn, and Ti as abundances in these regions, these results indicate that Mercury's surface is composed of FeS (1.16–3.98 wt%), CrS (0–0.89 wt%), TiS_2 (0–1.77 wt%), MnS (0–0.86 wt%), MgS (0–3.23 wt%), and CaS (0–0.33 wt%).

The other minerals in our derived mineralogies have modeled abundances that are too low for us to definitively claim their presence (i.e., the abundances could be attributed to uncertainties on the values used in our calculations – see Tables 1 and 2). These minerals include orthoclase (0.53–1.42 wt%), nepheline (0–3.10 wt%), corundum (0–0.80 wt%), titanite (0–1.35 wt%), and MnO (0–0.71 wt%). When we include the detection limits of Cr, Mn, and Ti in the oxide compositions, CrS, MnS, titanite, and MnO are produced (but these are not present when only the measured values of the elements are included). The presence of orthoclase in all the geochemical regions (albeit in small amounts) reflects that we included K in our compositions and orthoclase is the primary host for K (in hypersthene normative compositions) in our CIPW norm calculation. In reality, the K is likely a trace component in the abundant albitic plagioclase. Nepheline is only present in the HMR-CaS region, but we do not expect that it is an important part of Mercury's mineralogy because its abundance is within error of the reported values. Finally, we find that corundum is present in the HAl (as expected) and CB regions.

3.3. Petrologic classifications

We have also used the modal abundances of the calculated major silicate minerals to classify the geochemical regions according to IUGS standards, using the nomenclature and designations for plutonic rocks. Our classifications of igneous rock compositions exposed at the surface (for the NP-HMg, NP-LMg, PD, HMR, and HMR-CaS) are shown in Fig. 4. The clinopyroxene-orthopyroxene-olivine ternary (Fig. 4a) illustrates that the NP regions can be classified as either websterite or olivine websterites, mainly because of the high abundance of Na in these compositions. In addition, we classify the PD as a lherzolite, the HMR-CaS as a wehrlite, and the HMR as either a lherzolite or wehrlite (depending on the amount of Cr, Mn, and Ti present). Alternatively, when these same regions are shown on an olivine-plagioclase-pyroxene ternary (Fig. 4b), we find that they all fall within the olivine gabbronorite classification (except for the NP-LMg – without Cr, Mn, and Ti – which falls in the gabbronorite field).

The compositions of the geochemical regions are shown on a total alkali (Na_2O+K_2O) vs. silica (TAS) diagram in Fig. 5. According to this scheme, the NP-LMg is the most alkali-rich region and we classify it as a trachyandesite. We also find that the NP-HMg, HAl, and IT regions are basaltic andesites, the CB is an andesite, and both HMR compositions fall in the basalt field.

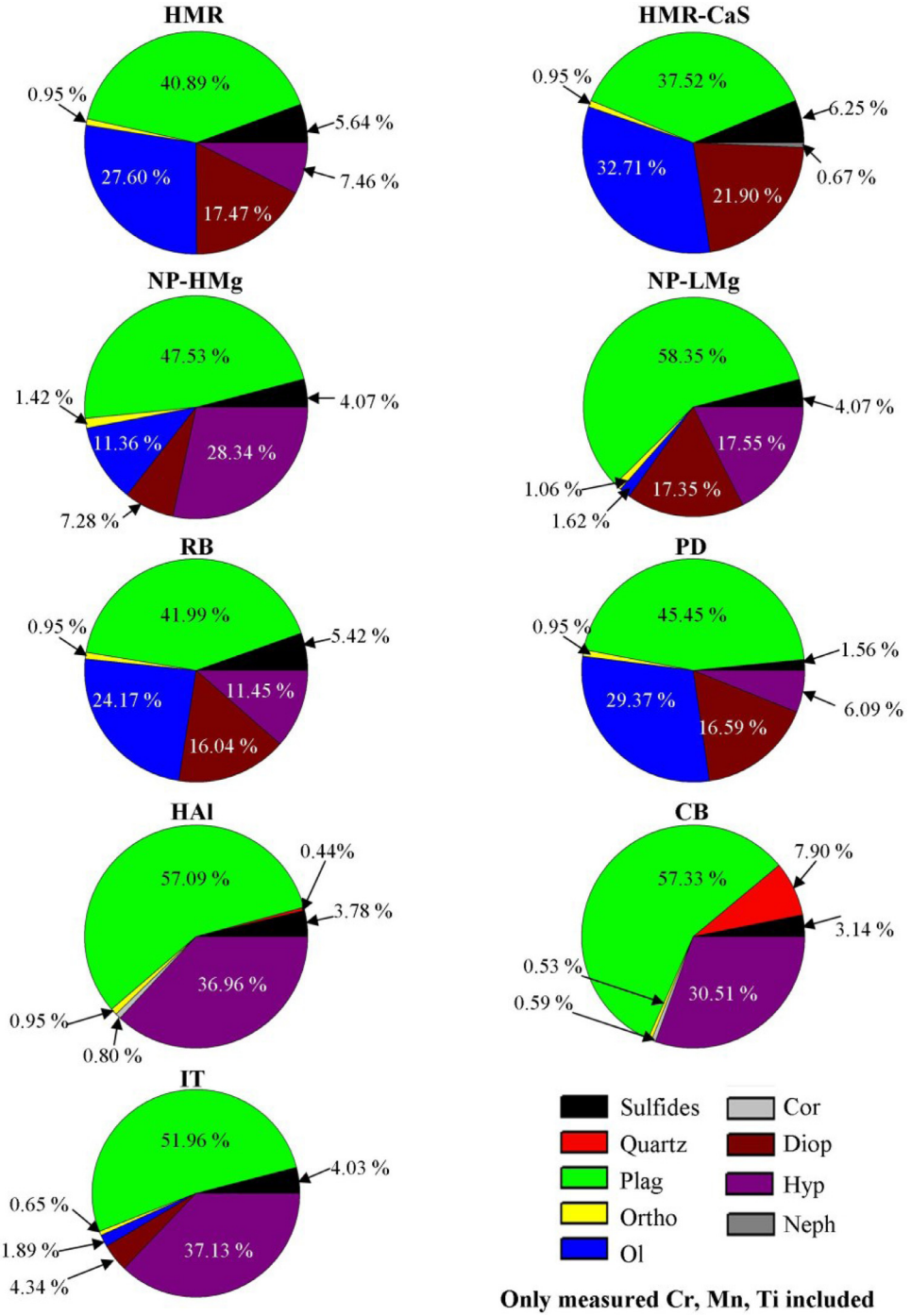

Fig. 2. Results of the CIPW normative calculations for each of the nine geochemical regions, for calculations where only measured values of Cr, Mn, and Ti are used (see Table 1). See Fig. S1 and Table 2 for normative calculations that include Cr, Mn, and Ti detection limits as abundances. Plag: plagioclase; Ortho: orthoclase; Ol: olivine; Cor: corundum; Diop: diopside; Hyp: hypersthene; Neph: nepheline.

The remaining regions (RB and PD) span the basalt/basaltic andesite boundary on the TAS diagram (depending on the amount of Cr, Mn, and Ti present). The TAS diagram, however, is not applicable to compositions with high MgO abundances (MgO >8 wt%, Le Bas, 2000) such as those found on Mercury (i.e., with MgO of 12.13–25.14 wt%). Consequently, we also used the high-Mg classification diagram (Le Bas, 2000) to place further constraints on the petrologic classifications. The high-Mg classification diagram is superimposed on the TAS diagram in Fig. 5 (i.e. shaded region with >52 wt% SiO_2) to illustrate the additional chemical boundaries and how they affect assigned nomenclature. With this additional classification, the CB, HAl, IT, and NP regions are classified as boninites (because their SiO_2 and MgO contents are >52 and 8 wt%, respectively). However, since the total alkali content for the NP-LMg extends beyond the upper bounds of this classification (≥4 wt% total alkalis), we use the term 'alkali-rich boninite' for this region's composition. This result is consistent with the classification of Vander Kaaden and McCubbin (2016). Both of the HMR regions are classified as alkali-rich komatiites (i.e., komatiites are defined as having ≤1 wt% Na_2O) because their SiO_2 contents are <52 wt% and their MgO contents are >18 wt%. Both the RB and PD can be classified as either boninitic or komatiitic, depending on the amount of SiO_2

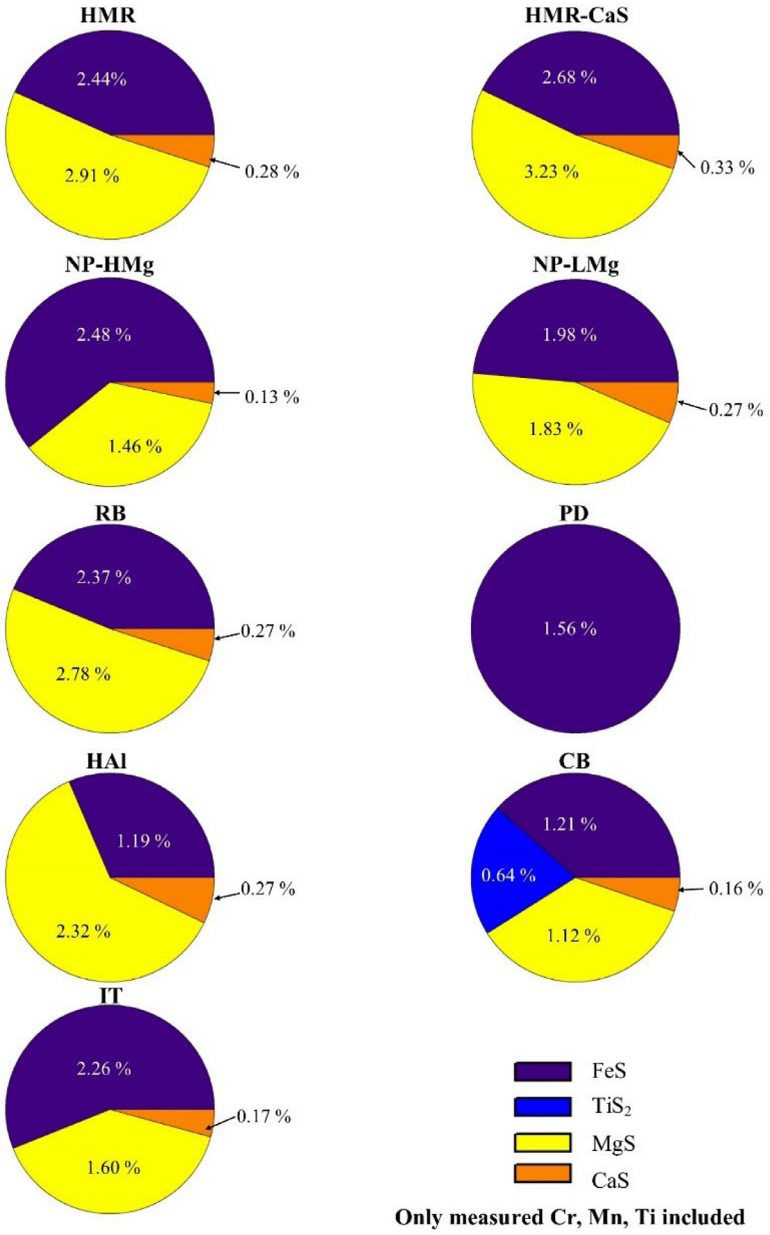

Fig. 3. Results of the CIPW normative sulfide calculations for the nine geochemical regions for a calculation where only the measured values for Cr, Mn, and Ti were used (see Table 1).

present (a direct result of the Cr, Mn, and Ti abundances in the compositions).

4. Discussion

4.1. Insights into mercury's mantle

In this section we focus on four of the nine geochemical units – the NP, PD, HMR, and HMR-CaS – that can provide insight into the planet's mantle and its igneous processes.

4.1.1. Melt compositions exposed at the surface

Geomorphic evidence supports the volcanic origin of both the northern plains and the pyroclastic deposit to the NE of Rachmaninoff Basin (e.g., Denevi et al., 2013; Head et al., 2011; Kerber et al., 2011; Kerber et al., 2009; Ostrach et al., 2015) and these regions are the best candidates for representative melt compositions, (i.e, exposed partial melts of Mercury's mantle). Indeed, the NP lavas are the most probable examples of actual melts that can be compositionally assessed from orbit (e.g., Denevi et al., 2013; Head et al., 2011; Vander Kaaden and McCubbin, 2015). However, we note that the NP is not a compositionally homogenous unit, and it consists of at least two distinct (in terms of Mg content) sub-terranes (Peplowski et al., 2015b; Weider et al., 2015). In addition, the NE Rachmaninoff PD is the largest pyroclastic deposit on Mercury's surface (Kerber et al., 2011; Thomas et al., 2014). Targeted XRS observations have been used to determine the chemical composition of this deposit (Weider et al., 2016). As this deposit is one of only a few on the planet that is not contained within an impact crater (Thomas et al., 2014), it is likely an example of partially melted mantle material on the surface of the planet. The pyroclastic nature of the deposit implies that some volatiles (e.g., C- and S-bearing species) were lost during the explosive volcanic episode from which it was produced (Kerber et al., 2011; Weider et al., 2016; Zolotov et al., 2013).

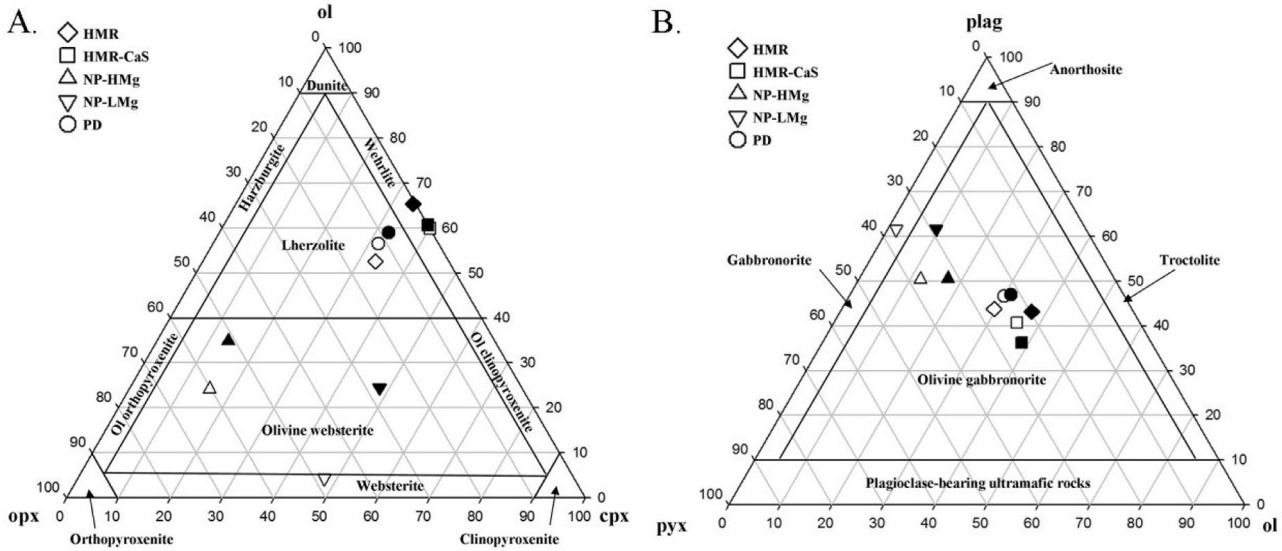

Fig. 4. IUGS rock classification diagrams for plutonic rocks. Results of the CIPW normative calculations of the silicate mineralogies for the HMR, HMR-CaS, NP-HMg, NP-LMg, and PD regions are shown on (A) the clinopyroxene (cpx)–olivine (ol)–orthopyroxene (opx) ternary and (B) the ol– plagioclase (plag)– pyroxene (pyx) ternary. Clinopyroxene and orthopyroxene are defined as the diopside and hypersthene components, respectively, in the CIPW normative mineralogy calculations (pyx in B is the sum of these values). Open symbols are for a calculation where only measured values of Cr, Mn, and Ti were considered and closed symbols are for a calculation where Cr, Mn, and Ti detection limits were used as upper limits.

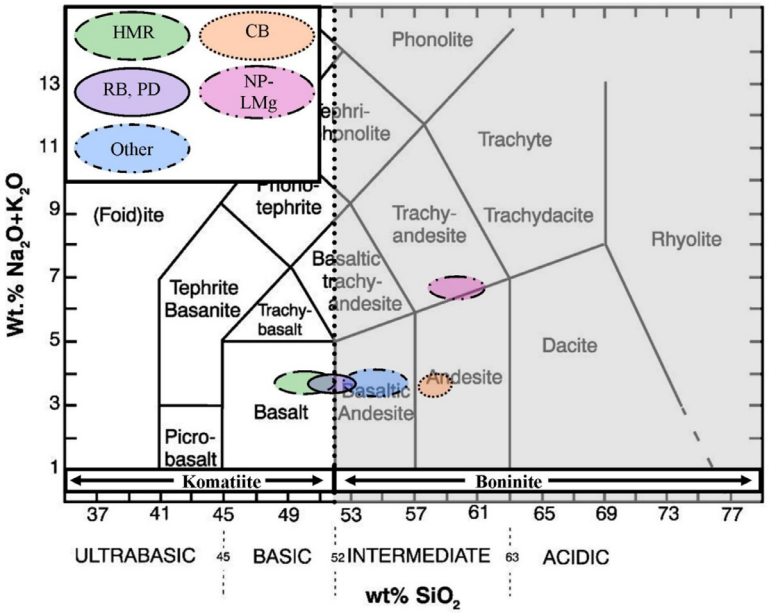

Fig. 5. Total alkali versus silica (TAS) diagram for the nine geochemical units (shown by colored ellipses). The HMR region (green ellipse) includes both the HMR and the HMR-CaS. The "Other" region (blue ellipse) includes the NP-HMg, Hal, and IT. Dashed line marks 52 wt% SiO_2. The shaded region to the right of this line (>52 wt% SiO_2) represents the boninite field and the unshaded region (<52 wt% SiO_2) indicates the komatiite field. (For interpretation of the references to color in this figure legend, the reader is referred to the web version of this article.)

Given that the NP and PD regions likely represent melt compositions, we have derived additional information regarding their geochemical properties (see Table 3). These data show that the NP-HMg composition is peraluminous (i.e., $Na_2O+K_2O+CaO < Al_2O_3$) and that the NP-LMg and PD compositions are metaluminous, i.e., $Al_2O_3 < (CaO+Na_2O+K_2O)$ and $Al_2O_3 > (Na_2O+K_2O)$. The low iron content of Mercury's surface results in high Mg# value's – i.e., molar (Mg/Mg+Fe)*100 – across the surface. Specifically, the Mg# for these three regions are consistently greater than 90 (i.e. range from 93–95 before removal of an FeS component). Furthermore, using the volatile-free compositions listed in Tables 1 and 2, the range in the ratio of non-bridging oxygens to tetrahedrally coordinated cations in the melts (NBO/T) that we calculate illustrates that the NP-LMg lavas are typically polymerized (NBO/T<1) melts and are therefore more viscous than the PD (which is less polymerized than the NP, i.e., NBOT/T>1). Our NBO/T value for the NP-LMg is consistent with the experimental results of Sehlke and Whittington (2015), which indicates that the NP lavas are more viscous than Hawaiian basalts erupted at the same temperature (Sehlke and Whittington, 2015; Sehlke et al., 2014).

Our calculated normative mineralogies for the NP regions (i.e., dominated by plagioclase, diopside, hypersthene, and olivine, with lesser amounts of orthoclase, sulfides, and MnO) are consistent

Table 3
Calculated silicate melt parameters for three of the geochemical regions (those thought to have a volcanic origin). M: Metaluminous, i.e., ($CaO+Na_2O+K_2O$) > Al_2O_3 > (Na_2O+K_2O). P: Peraluminous, i.e., Na_2O+K_2O+CaO < Al_2O_3. NBO/T: Non-bridging oxygen per tetrahedrally coordinated cation.

	NP-HMg	NP-LMg	PD
Alumina Saturation	P	M	M
Mg # (molar $(\frac{Mg}{Mg+Fe})*100$)	~95	~93	~95
Alkalinity Index	~0.5	~0.9	~0.5
NBO/T	~1	~0.7	~1.2

with the experimental results of Vander Kaaden and McCubbin (2016) that showed the NP boninites were derived from high degrees of partial melting of an olivine-dominant, pyroxene- and plagioclase-bearing mantle source region. Given that the abundance of Na reported for the PD is latitudinally binned between 30–45°, it may not represent the actual abundance of Na in the PD given its small area and depletion in S, which is a moderately volatile element like Na. However, assuming that the reported Na abundance is appropriate, we find that the PD consistently plots away from the NP regions, in terms of normative mineralogy and rock type (Figs. 4 and 5). This suggests that either Mercury's mantle is laterally heterogeneous or that the PD material erupted from greater depths than the NP material (i.e., where there was less plagioclase in the source). The formation of MnO in our normative mineralogy for the PD is caused by an S deficit, which is consistent with the proposed loss of S-bearing volatiles during the pyroclastic eruption (Weider et al., 2016).

4.1.2. High-Mg region

The HMR, centered at ~30°N, 290°E, is a large (>5×10^6 km^2) area with the highest Mg/Si, S/Si, and Ca/Si ratios on the planet (i.e., the HMR-CaS), as well as relatively low Al/Si values (Weider et al., 2015). The HMR also has low topography and thin crust relative to the rest of Mercury (Weider et al., 2015). However, the origin of the HMR has yet to be determined. Weider et al., (2015) suggested that the region's komatiitic composition could be indicative of high-degree partial melting of a lherzolitic mantle source, or that the HMR is an impact-related feature and its high Mg/Si was caused by mantle excavation during a very large impact event more than 4.1 Ga ago.

Our classification of the HMR as a komatiite is consistent with that of Maturilli et al., (2014), who have suggested that Commondale (a komatiite) is the most accurate terrestrial analogue for the region. The mineralogy of Commondale is dominated by orthopyroxene instead of clinopyroxene, and its lavas have high SiO_2, low Fe, and high CaO/Al_2O_3 (Wilson, 2003), similar to the chemical composition of the HMR. If the difference in normative mineralogy that we derive for the HMR and HMR-CaS (i.e., hypersthene-normative and nepheline-normative, respectively) is correct, it would have important consequences for understanding the mineralogical heterogeneity of Mercury's interior. Given the margin of error, however, we cannot consider this difference significant. We find that both the HMR and HMR-CaS plot close to the PD in Fig. 4a and b. Therefore the HMR regions may have been produced in a similar manner as the PD, i.e., from a deeper source region, or from higher degrees of partial melting, than the NP. On the basis of our results, it is clear that both HMR compositions represent igneous material (i.e. volcanic or impact melt). This is consistent with the results of Frank et al., (2016), who suggested that impact-excavation of mantle material is unlikely to be the cause of the HMR's high Mg content, though the influence of an impact cannot be definitively ruled out. With our work, we cannot determine if the HMR's volcanism was induced by impact(s) or partial melting of the mantle.

4.2. Comparative planetary geochemistry

4.2.1. Lithological diversity

To determine the true extent of Mercury's petrologic diversity, we have compared our data to other terrestrial bodies, i.e., Earth (Lebas et al., 1986), the Moon (Lodders and Fegley, 1998), Mars (Gellert et al., 2006; McSween et al., 2009; Santos et al., 2015; Stolper et al., 2013), and Vesta (Barrat et al., 2009; Lodders and Fegley, 1998; Mittlefehldt, 2015). Although our derived Mercury compositions are classified individually in Fig. 5, we have plotted the full range of mercurian compositions as a single field on the TAS diagram in Fig. 6 to facilitate a direct comparison with other planets. In this diagram, the terrestrial rocks span the entire range (because the TAS classification is based on rocks from Earth). With the exception of lunar granites (i.e., sample 12,032,366–19; Seddio et al., 2013), lunar rocks have – on average – less than 0.5 wt% total alkalis. Although they span a relatively wide range in SiO_2 content (~20 wt% SiO_2), their consistently low Na_2O+K_2O implies that the lunar rocks are constrained to a small range of volcanic rock types. The data for Vesta were compiled from eucrite basalt samples and impact glasses from howardites (Barrat et al., 2009; Lodders and Fegley, 1998). With the exception of two impact glasses that are enriched in alkalis and SiO_2 (shown as small purple circles in the dacite field in Fig. 6), igneous rocks from Vesta span a very small range in total alkali content (≤3 wt%) and SiO_2 (≤9 wt%). For Mars, we compiled orbital (Mars Odyssey), rover (Mars Exploration Rover, Mars Science Laboratory), and martian meteorite (NWA 7034, SNC's) data. Despite the large quantity of Mars data, it is apparent from Fig. 6 that they span only a small compositional field (i.e., ≤6 wt% total alkalis and ≤16 wt% SiO_2). An exception is the so-called 'Jake M' rock (analyzed with the Mars Science Laboratory), which plots in the phono-tephrite field and has been classified as a mugearite (Stolper et al., 2013). This rock is significantly different from other martian meteorites and rocks, but it is evidence of alkaline magmas on Mars (McCubbin et al., 2016; McSween et al., 2006; Nekvasil et al., 2007, 2009; Stolper et al., 2013).

Mercury is the only one of these planetary bodies for which we do not currently have a known hand sample available for analysis on Earth. The illustrated range in alkali and SiO_2 contents is thus derived entirely from MESSENGER results, which have substantial areal footprints. Consequently, there is likely a sampling bias when comparing the dataset for Mercury to the datasets for the other bodies because diversity tends to increase with increasing spatial resolution. For example, geochemical variations on the surface of Mars as measured by the GRS on Mars Odyssey are minor (Boynton et al., 2007; Karunatillake et al., 2009) in comparison to the diversity in rocks analyzed *in-situ* by rovers (McSween et al., 2006; Sautter et al., 2016; Schmidt et al., 2014). Our petrologic classification of the nine geochemical regions indicates that Mercury's surface is chemically evolved relative to those of the Moon, Mars, and Vesta, and it exhibits a substantial range in geochemical diversity (with respect to SiO_2), despite the low spatial resolution that orbital XRS and GRS provide compared to *in-situ* analysis. Future *in-situ* analyses of rocks on the mercurian surface may reveal a lithologic diversity that matches or even surpasses that of the Earth.

4.2.2. Mantle melting scenarios

The NP-HMg, NP-LMg, and PD regions – i.e., the most likely examples of surface compositions that represent the compositions of silicate melts on Mercury's surface (see Section 4.1.1)—have similar characteristics to terrestrial silicate melts, albeit with some very important differences. As described in Section 3.3, using a TAS diagram, we classify the presumed igneous rocks of these regions as boninites. On Earth, arc magmatism and hydrous conditions

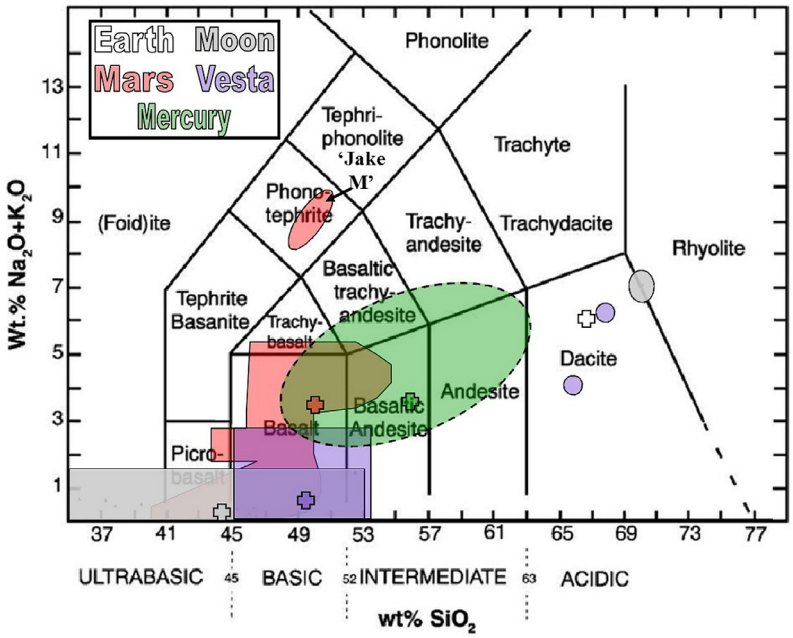

Fig. 6. TAS diagram showing the petrological classifications of rocks on the Moon, Earth, Mars, Vesta, and Mercury. The Mercury ellipse encloses the results shown in Fig. 5. Data for Mars, the Moon, and Vesta are taken from Barrat et al., (2009), Gellert et al., (2006), Lodders and Fegley (1998), McSween et al., (2009), and Stolper et al., (2013). The terrestrial rocks (unshaded) span the entire diagram. Crosses represent the average surface compositions given in Table 4.

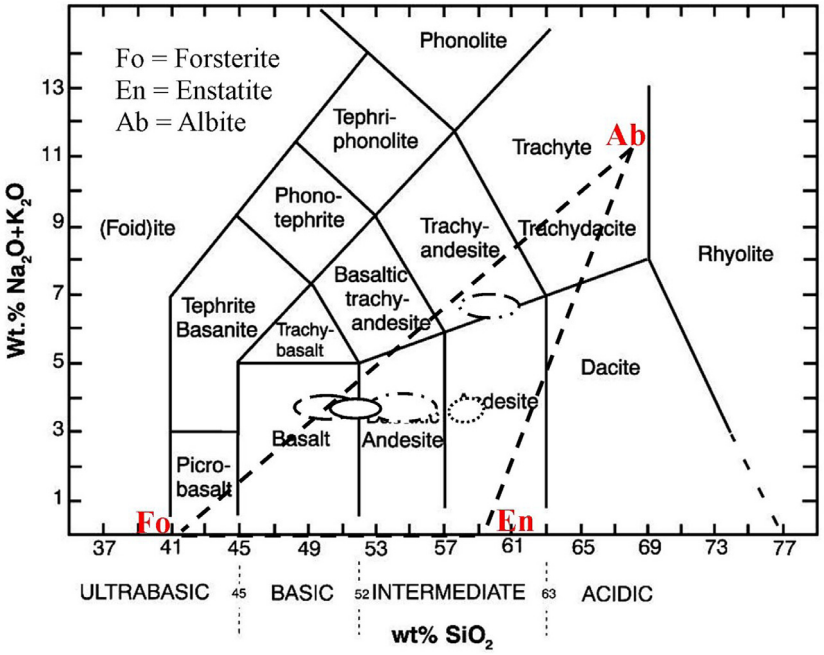

Fig. 7. TAS diagram with a superimposed triangle of the endmember minerals forsterite (Fo), enstatite (En), and Albite (Ab). Fields for the Mercury geochemical regions are the same as those shown in Fig. 5.

are typically required to produce boninites (e.g., Cameron et al., 1983; Polat et al., 2002). In contrast, Vander Kaaden and McCubbin (2016) demonstrated eruption scenarios for the NP in which high degrees of partial melting from a shallow source region (similar to flood volcanism on Earth) were invoked. In other words, even in the absence of arc magmatism and hydrous conditions, large volumes of boninitic lavas can be produced on Mercury's surface. Furthermore, we show in Fig. 7 that the compositions of the majority of our geochemical regions fall within a forsterite–enstatite–albite triangle on the TAS diagram. Our results indicate that Mercury's interior is probably made of the same major rock-forming minerals as other planetary mantles.

4.2.3. Average surface composition

The IT, which consists of Mercury's southern hemisphere and otherwise undefined areas of the northern hemisphere, is assumed to be a good representation of the planet's average crust due to the large size of measurement footprints in the southern hemisphere. Within the IUGS classification scheme, we find that the IT falls very close to the komatiite–boninite boundary. In terms of its mineralogical components, we find that the IT is most similar to the HAl and CB regions (Fig. 2), containing greater than 50% plagioclase, 30% hypersthene, and 3% sulfides. Additionally, the IT is hypersthene- and olivine-normative, like the majority of our geochemical regions. In contrast, our normative mineralogy results

Table 4
Composition of representative 'average' surface compositions for the Moon (Korotev et al., 2003), Mars (Santos et al., 2015), Earth (Rudnick and Gao, 2003), Vesta (Mittlefehldt, 2015; Mittlefehldt et al., 2013; Warren et al., 2009), and Mercury (this study). The Mercury value is taken from the composition of the IT region (see Table 1).

Oxide	Moon	Mars	Earth	Vesta	Mercury
SiO_2	44.80	50.40	66.45	49.62	55.89
MgO	5.41	12.19	2.47	13.79	17.94
CaO	16.34	5.73	3.58	7.14	5.74
Al_2O_3	28.26	11.10	15.36	8.69	14.06
K_2O	0.03	0.54	2.79	0.30	0.11
Na_2O	0.35	3.03	3.26	0.31	3.51
FeO	4.41	14.94	5.03	18.34	1.84
TiO_2	0.22	0.70	0.64	0.44	0
Cr_2O_3	0.10	0.00	0.13	0.63	0
MnO	0.06	0.35	0.10	0.53	0
P_2O_5	0.03	1.01	0.15	0.06	0
S	0.00	0.00	0.06	0.29	1.81
-O = S	0.00	0.00	0.03	0.14	0.9
Total	100.00	100.00	100.00	100.00	100.00

Table 5
Composition of regolith for the Moon (Korotev et al., 2003), Mars (Santos et al., 2015), Earth (Rudnick and Gao, 2003), Vesta (Mittlefehldt, 2015; Mittlefehldt et al., 2013; Warren et al., 2009) and Mercury (this study) renormalized once all FeO is removed.

Oxide	Moon	Mars	Earth	Vesta	Mercury
SiO_2	46.86	59.26	69.98	60.76	56.94
MgO	5.66	14.33	2.60	16.89	18.28
CaO	17.09	6.74	3.77	8.74	5.85
Al_2O_3	29.56	13.05	16.18	10.65	14.32
K_2O	0.03	0.63	2.94	0.37	0.11
Na_2O	0.37	3.56	3.43	0.38	3.58
FeO	*0.00*	*0.00*	*0.00*	*0.00*	*0.00*
TiO_2	0.23	0.82	0.67	0.53	0.00
Cr_2O_3	0.10	0.00	0.14	0.77	0.00
MnO	0.06	0.41	0.11	0.65	0.00
P_2O_5	0.03	1.19	0.16	0.07	0.00
S	0.00	0.00	0.06	0.36	1.84
-O =S	0.00	0.00	0.03	0.18	0.92
Total	100.00	100.00	100.00	100.00	100.00

show that the IT contains more orthopyroxene than other regions on Mercury and typically contains more plagioclase (with the exception of the NP-LMg, HAl, and CB regions). The IT also has a similar abundance of sulfides to the other geochemical regions, with the exception of the PD (Fig. 2) that most likely lost a majority of its S during explosive volcanism (Weider et al., 2016), suggesting an even distribution of sulfur across the planet. Since the IT region composes the majority of Mercury's surface (see Fig. 1), it is possible to say that plagioclase and orthopyroxene dominate the surface materials, with lesser amounts of clinopyroxene, sulfides, olivine, and silica. In addition, the olivine-normative nature of the IT indicates that silica exists in Mercury's regolith at lower abundances than olivine. These results are consistent with those of Stockstill-Cahill et al., (2012), who showed the surface of Mercury is mainly composed of Mg-rich orthopyroxene and plagioclase.

To compare this Mercury 'average' surface composition with that of other planetary bodies, we have considered representative regolith compositions for the Moon, Mars, and Vesta, as well as a suitable upper crust composition for the Earth (see Table 4 and Fig. 6). We used the average lunar regolith composition of Korotev et al., (2003), which was derived from lunar meteorite data. This composition is dominated by that of the feldspathic highlands terrane, which is sufficiently far away from the lunar mare and procellarum KREEP terrane that it is representative of the average lunar crust. The martian regolith composition was derived from the bulk matrix composition of the martian regolith breccia NWA 7034 (Santos et al., 2015), which is thought to be the most representative sample of the martian crust available (i.e., Beck et al., 2015; Agee et al., 2013). We calculated the Vesta regolith composition from the average of regolithic howardities, i.e., Bholghati, Bununu, Jodzie, Kapoeta, Malvern, EET 87,513, GRO 95,535, GRO 95,602, LEW 85,313, and MET 00,423 (Mittlefehldt, 2015; Mittlefehldt et al., 2013; Warren et al., 2009). We used the suggested composition of Rudnick and Gao (2003) to represent Earth's upper crust. Our comparison of the average compositions of these planetary bodies shows that Mercury (i.e., the IT) has the highest concentrations of MgO, Na_2O, and S, and the lowest FeO. The other oxides (e.g., SiO_2, CaO, Al_2O_3, and K_2O) are intermediate among the terrestrial compositions.

We have also calculated a normative mineralogy for each of the other planetary compositions (Table S4). These results suggest that there are similar minerals present on the surface of all these bodies (i.e., plagioclase, orthoclase, diopside, and hypersthene). However, while ilmenite and apatite are present on Earth, Mars, and the Moon, they are likely absent from Mercury's surface mineralogy (Evans et al., 2015; Riner et al., 2010, 2011; Fig. 2). The high SiO_2 abundance of the IT (greater than for the other terrestrial bodies we have considered, with the exception of the Earth) gives the impression that Mercury is an evolved planetary body. It is thought that the Earth obtained its Si-rich surface composition through plate tectonics and processes involving liquid water (Campbell and Taylor, 1983), but Mercury's apparently evolved nature must have arisen without such processes because Mercury is too reducing to support the formation of H_2O (McCubbin et al., 2012). We infer, however, that Mercury's high surface SiO_2 abundance is a primitive signature and a direct consequence of the planet's low oxygen fugacity. Under such highly reducing conditions, the majority of Fe in the planet will partition into the core (Hauck et al., 2013) and little will remain in the silicate portion. When such a major oxide component (i.e., FeO) is removed from the silicate, all other components must increase proportionally. SiO_2 is therefore the most affected because it is the most abundant oxide component. It is important to note that some Si is also lost to the core because of the highly reducing conditions (Malavergne et al., 2004), but this process primarily increases the Mg/Si ratio of the bulk silicate. Indeed, this is a good explanation for Mercury's primary mantle mineral being forsterite rather than enstatite (Vander Kaaden and McCubbin, 2016). To better illustrate the bulk compositional effect of FeO removal, we renormalized all the compositions in Table 4 after FeO had been removed (see Table 5). After this calculation, we find that Mercury's SiO_2 content is only greater than that of the Moon and is much more consistent with the other bodies. Overall, our results (Table 4) clearly show that Mercury is a geochemical endmember among terrestrial planetary bodies, and that Mercury's low oxygen fugacity gave rise to a unique surface composition.

5. Conclusion

In this study we have identified nine geochemical regions across Mercury's surface and have used MESSENGER XRS and GRNS data to assign them elemental compositions. We used these compositions to derive a normative mineralogy for each region and to make petrologic classifications. We infer a wide range of SiO_2 content, alkali content, and major element compositions across Mercury's surface, and our results indicate that Mercury's surface consists of a diverse set of rocks (with the potential for a greater level of diversity compared with other terrestrial bodies). Our CIPW normative calculations indicate that the surface is dominated by plagioclase, pyroxene, and olivine, with minor amounts of quartz. Although these minerals are similar to those found on other plan-

etary bodies, their specific chemical compositions on Mercury are vastly different, (most notably the low abundance of Fe, and high abundance of Na and Mg). Further experimental investigations, particularly of the unique geochemical units such as the NP and PD, are warranted to place constraints on the thermal and magmatic evolution of Mercury as well as the physical and chemical properties of the planet (e.g. determination of surface and mantle mineralogy; Charlier et al., 2013; Namur et al., 2016; Vander Kaaden and McCubbin, 2015, 2016). From our petrologic classifications, we find that the nine geochemical regions can generally be assigned as komatiites or boninites. In fact, Mercury may represent the only planet, other than Earth, with large amounts of andesitic crust (i.e., with relatively high SiO_2) exposed at the surface. Although the evolved nature of Earth's crust is associated with plate tectonics and the presence of water, these factors are not relevant to Mercury and its high surface SiO_2 is thus a primitive feature related to its low oxygen fugacity. Our study of Mercury's surface compositions therefore provides important new insights into Mercury's mantle as well as crustal evolution mechanisms in our solar system.

Acknowledgments

We thank the MESSENGER Science Team, with special thanks to the MESSENGER Geochemistry Discipline Group, for fruitful discussions regarding the interpretation of MESSENGER data and preparation of this manuscript. We also thank Ryan Zeigler, Randy Korotev, Alison Santos, and Dave Mittlefehldt for helpful discussions regarding lunar, martian, and vestan chemical compositions. This manuscript benefitted from thoughtful reviews by Justin Filiberto and Rachel Klima as well as editorial handling by Oded Aharonson. This work was funded by a NASA Solar System Workings Grant NNX16AK39G to FMM. This work was also supported by NASA Headquarters under the NASA Earth and Space Science Fellowship Program-Grant NNX15AQ80H awarded to KEVK.

Supplementary materials

Supplementary material associated with this article can be found, in the online version, at doi:10.1016/j.icarus.2016.11.041.

References

Agee, C.B., Wilson, N.V., McCubbin, F.M., Ziegler, K., Polyak, V.J., Sharp, Z.D., Asmerom, Y., Nunn, M.H., Shaheen, R., Thiemens, M.H., Steele, A., Fogel, M.L., Bowden, R., Glamoclija, M., Zhang, Z., Elardo, S.M., 2013. Unique meteorite from early amazonian Mars: water-rich basaltic breccia northwest africa 7034. Science 339, 780–785.

Albarède, F., 2009. Volatile accretion history of the terrestrial planets and dynamic implications. Nature 461, 1227–1233.

Barrat, J.A., Bohn, M., Gillet, P., Yamaguchi, A., 2009. Evidence for K-rich terranes on vesta from impact spherules. Meteorit. Planet Sci. 44, 359–374.

Beck, P., Pommerol, A., Zanda, B., Remusat, L., Lorand, J.P., Göpel, C., Hewins, R., Pont, S., Lewin, E., Quirico, E., Schmitt, B., Montes-Hernandez, G., Garenne, A., Bonal, L., Proux, O., Hazemann, J.L., Chevrier, V.F., 2015. A noachian source region for the "Black Beauty" meteorite, and a source lithology for mars surface hydrated dust. Earth Planet. Sci. Lett. 427, 104–111.

Blair, D.M., Freed, A.M., Byrne, P.K., Klimczak, C., Prockter, L.M., Ernst, C.M., Solomon, S.C., Melosh, H.J., Zuber, M.T., 2013. The origin of graben and ridges in Rachmaninoff, Raditladi, and mozart basins, mercury. J. Geophys. Res.: Planets 118, 47–58.

Blewett, D.T., Hawke, B.R., Lucey, P.G., 2002. Lunar pure anorthosite as a spectral analog for mercury. Meteorit. Planet. Sci. 37, 1255–1268.

Blewett, D.T., Lucey, P.G., Hawke, B.R., Ling, G.G., Robinson, M.S., 1997. A comparison of mercurian reflectance and spectral quantities with those of the Moon. Icarus 129, 217–231.

Blewett, D.T., Robinson, M.S., Denevi, B.W., Gillis-Davis, J.J., Head, J.W., Solomon, S.C., Holsclaw, G.M., McClintock, W.E., 2009. Multispectral images of Mercury from the first MESSENGER flyby: Analysis of global and regional color trends. Earth Planet. Sci. Lett. 285, 272–282.

Boynton, W.V., Taylor, G.J., Evans, L.G., Reedy, R.C., Starr, R., Janes, D.M., Kerry, K.E., Drake, D.M., Kim, K.J., Williams, R.M.S., Crombie, M.K., Dohm, J.M., Baker, V., Metzger, A.E., Karunatillake, S., Keller, J.M., Newsom, H.E., Arnold, J.R., Brückner, J., Englert, P.A.J., Gasnault, O., Sprague, A.L., Mitrofanov, I., Squyres, S.W., Trombka, J.I., d'Uston, L., Wanke, H., Hamara, D.K., 2007. Concentration of H, Si, Cl, K, Fe, and th in the low- and mid-latitude regions of mars. J. Geophys. Res.-Planets 112.

Broadfoot, A.L., Kumar, S., Blelton, M.J.S., McElroy, M.B., 1974. Mercury's atmosphere from mariner 10: preliminary results. Science 185, 166–169.

Broadfoot, A.L., Shemansky, D.E., Kumar, S., 1976. Mariner 10: mercury atmosphere. Geophys. Res. Lett. 3, 577–580.

Brown, S.M., Elkins-Tanton, L.T., 2009. Compositions of mercury's earliest crust from magma ocean models. Earth Planet. Sci. Lett. 286, 446–455.

Bruck Syal, M., Schultz, P.H., Riner, M.A., 2015. Darkening of mercury's surface by cometary carbon. Nat. Geosci. 8, 352–356.

Burns, R.G., 1993. Mineralogical Applications of Crystal Field Theory. Cambridge University Press, New York, p. 551.

Cameron, W.E., McCulloch, M.T., Walker, D.A., 1983. Boninite Petrogenesis: chemical and nd-sr isotopic constraints. Earth Planet. Sci. Lett. 65, 75–89.

Campbell, I.H., Taylor, S.R., 1983. No water, no granites - No oceans, no continents. Geophys. Res. Lett. 10, 1061–1064.

Charlier, B., Grove, T.L., Zuber, M.T., 2013. Phase equilibria of ultramafic compositions on mercury and the origin of the compositional dichotomy. Earth Planet. Sci. Lett. 363, 50–60.

Chase, S.C., Miner, E.D., Morrison, D., Munch, G., Neugebauer, G., Schroeder, M., 1974. Preliminary infrared radiometry of the night side of mercury from mariner 10. Science 185, 142–145.

Cross, W., Iddings, J.P., Pirsson, L.V., Washington, H.S., 1903. Quantitative Classification of Igneous Rocks. University of Chicago Press.

Denevi, B.W., Ernst, C.M., Meyer, H.M., Robinson, M.S., Murchie, S.L., Whitten, J.L., Head, J.W., Watters, T.R., Solomon, S.C., Ostrach, L.R., Chapman, C.R., Byrne, P.K., Klimczak, C., Peplowski, P.N., 2013. The distribution and origin of smooth plains on mercury. J. Geophys. Res.: Planets 118, 891–907.

Evans, L.G., Peplowski, P.N., McCubbin, F.M., McCoy, T.J., Nittler, L.R., Zolotov, M.Y., Ebel, D.S., Lawrence, D.J., Starr, R.D., Weider, S.Z., Solomon, S.C., 2015. Chlorine on the surface of Mercury: MESSENGER gamma-ray measurements and implications for the planet's formation and evolution. Icarus 257, 417–427.

Evans, L.G., Peplowski, P.N., Rhodes, E.A., Lawrence, D.J., McCoy, T.J., Nittler, L.R., Solomon, S.C., Sprague, A.L., Stockstill-Cahill, K.R., Starr, R.D., Weider, S.Z., Boynton, W.V., Hamara, D.K., Goldsten, J.O., 2012. Major-element abundances on the surface of Mercury: results from the MESSENGER gamma-ray spectrometer. J. Geophys. Res.-Planets 117, E00L07.

Frank, E.A., Potter, R.W.K., Abramov, O., Mojzsis, S.J., Nittler, L.R., 2016. Investigations into the origin of mercury's high-magnesium region. In: Proceedings of 47th Lunar and Planetary Science Conference. The Woodlands, TX, p. 1270.

Gellert, R., Rieder, R., Bruckner, J., Clark, B.C., Dreibus, G., Klingelhofer, G., Lugmair, G., Ming, D.W., Wanke, H., Yen, A., Zipfel, J., Squyres, S.W., 2006. Alpha particle X-ray spectrometer (APXS): results from gusev crater and calibration report. J. Geophys. Res.-Planets 111.

Hapke, B., 1977. Interpretations of optical observations of mercury and the moon. Phys. Earth Plenet. Int. 15, 264–274.

Hauck, S.A., Margot, J.L., Solomon, S.C., Phillips, R.J., Johnson, C.L., Lemoine, F.G., Mazarico, E., McCoy, T.J., Padovan, S., Peale, S.J., Perry, M.E., Smith, D.E., Zuber, M.T., 2013. The curious case of mercury's internal structure. J. Geophys. Res. - Planets 118, 1204–1220.

Head, J.W., Chapman, C.R., Strom, R.G., Fassett, C.I., Denevi, B.W., Blewett, D.T., Ernst, C.M., Watters, T.R., Solomon, S.C., Murchie, S.L., Prockter, L.M., Chabot, N.L., Gillis-Davis, J.J., Whitten, J.L., Goudge, T.A., Baker, D.M.H., Hurwitz, D.M., Ostrach, L.R., Xiao, Z., Merline, W.J., Kerber, L., Dickson, J.L., Oberst, J., Byrne, P.K., Klimczak, C., Nittler, L.R., 2011. Flood volcanism in the northern high latitudes of mercury revealed by MESSENGER. Science 333, 1853–1856.

Herd, C.D.K., 2008. Basalts as probes of planetary interior redox state. Oxyg. Solar Syst. 68, 527–553.

Johannsen, A., 1931. A Descriptive Petrography of the Igneous Rocks. University of Chicago Press, pp. 88–92.

Karunatillake, S., Wray, J.J., Squyres, S.W., Taylor, G.J., Gasnault, O., McLennan, S.M., Boynton, W., El Maarry, M.R., Dohm, J.M., 2009. Chemically striking regions on mars and stealth revisited. J. Geophys. Res.-Planets 114.

Kerber, L., Head, J.W., Blewett, D.T., Solomon, S.C., Wilson, L., Murchie, S.L., Robinson, M.S., Denevi, B.W., Domingue, D.L., 2011. The global distribution of pyroclastic deposits on Mercury: the view from MESSENGER flybys 1-3. Planet. Space Sci. 59, 1895–1909.

Kerber, L., Head, J.W., Solomon, S.C., Murchie, S.L., Blewett, D.T., Wilson, L., 2009. Explosive volcanic eruptions on Mercury: eruption conditions, magma volatile content, and implications for interior volatile abundances. Earth Planet. Sci. Lett. 285, 263–271.

Korotev, R.L., Jolliff, B.L., Zeigler, R.A., Gillis, J.J., Haskin, L.A., 2003. Feldspathic lunar meteorites and their implications for compositional remote sensing of the lunar surface and the composition of the lunar crust. Geochim Cosmochim Acta 67, 4895–4923.

Lawrence, D.J., Feldman, W.C., Goldsten, J.O., Maurice, S., Peplowski, P.N., Anderson, B.J., Bazell, D., McNutt Jr., R.L., Nittler, L.R., Prettyman, T.H., Rodgers, D.J., Solomon, S.C., Weider, S.Z., 2013. Evidence for water ice near mercury's north pole from MESSENGER neutron spectrometer measurements. Science 339, 292–298.

Lawrence, D.J., Feldman, W.C., Goldsten, J.O., McCoy, T.J., Blewett, D.T., Boynton, W.V., Evans, L.G., Nittler, L.R., Rhodes, E.A., Solomon, S.C., 2010. Identification and measurement of neutron-absorbing elements on mercury's surface. Icarus 209, 195–209.

Lawrence, D.J., Peplowski, P.N., Beck, A.W., Feldman, W.C., Frank, E.A., McCoy, T.J., Nittler, L.R., Chabot, N.L., Ernst, C.M., Solomon, S.C., 2017. Compositional terranes on Mercury: information from fast neutrons. Icarus 281, 32–45.
Le Bas, M.J., 2000. IUGS reclassification of the high-mg and picritic volcanic rocks. J. Petrol. 41, 1467–1470.
Le Maitre, R.W., Streckeisen, A., Zanettin, B., Le Bas, M.J., Bonin, B., Bateman, P., Bellieni, G., Dudek, A., Efremova, S., Keller, J., Lameyre, J., Sabine, P.A., Schmid, R., Sorensen, H., Woolley, A.R., 2002. Igneous Rocks: A Classification and Glossary of Terms. Cambridge University Press, New York.
Lebas, M.J., Lemaitre, R.W., Streckeisen, A., Zanettin, B., 1986. A chemical classification of volcanic-rocks based on the total alkali silica diagram. J. Petrol. 27, 745–750.
Lodders, K., Fegley, B., 1998. The Planetary Scientist's Compendium. Oxford University Press, New York.
Maturilli, A., Helbert, J., St. John, J.M., Head, J.W.I., Vaughan, W.M., D'Amore, M., Gottschalk, M., Ferrari, S., 2014. Komatiites as mercury surface analogues: spectral measurements at PEL. Earth Planet. Sci. Lett. 398, 58–65.
Malavergne, V., Siebert, J., Guyot, F., Gautron, L., Combres, R., Hammouda, T., Borensztajn, S., Frost, D., Martinez, I., 2004. Si in the core? New high-pressure and high-temperature experimental data. Geochim Cosmochim Acta 68 (20), 4201–4211.
McClintock, W.E., Izenberg, N.R., Holsclaw, G.M., Blewett, D.T., Domingue, D.L., Head, J.W., Helbert, J., McCoy, T.J., Murchie, S.L., Robinson, M.S., Solomon, S.C., Sprague, A.L., Vilas, F., 2008. Spectroscopic observations of Mercury's surface reflectance during MESSENGER's first Mercury Flyby. Science 321 (5885), 62–65.
McCord, T.B., Clark, R.N., 1979. The Mercury soil: Presence of Fe^{2+}. J. Geophys. Res.: Solid Earth 84 (B13), 7664–7668.
McCubbin, F.M., Riner, M.A., Vander Kaaden, K.E., Burkemper, L.K., 2012. Is mercury a volatile-rich planet? Geophys. Res. Lett. 39.
McCubbin, F.M., Boyce, J.W., Szabó, T., Santos, A.R., Tartèse, R., Domokos, G., Vazquez, J., Keller, L.P., Moser, D.E., Jerolmack, D.J., Shearer, C.K., Muttik, N., Steele, A., Elardo, S.M., Rahman, Z., Anand, M., Delhaye, T., Agee, C.B., 2016. Geologic history of martian regolith breccia northwest africa 7034: evidence for hydrothermal activity and lithologic diversity in the martian crust. J. Geophys. Res.-Planets 121. doi:10.1002/2016JE005143.
McSween, H.Y., Ruff, S.W., Morris, R.V., Bell, J.F., Herkenhoff, K.E., Gellert, R., Stockstill, K.R., Tornabene, L.L., Squyres, S.W., Crisp, J.A., Christensen, P.R., McCoy, T.J., Mittlefehldt, D.W., Schmidt, M., 2006. Alkaline volcanic rocks from the columbia Hills, gusev crater, mars. J. Geophys. Res. - Planets 111, 15.
McSween, H.Y., Taylor, G.J., Wyatt, M.B., 2009. Elemental composition of the martian crust. Science 324, 736–739.
Mittlefehldt, D.W., 2015. Asteroid (4) Vesta: I. The howardite-eucrite-diogenite (HED) clan of meteorites. Chemi der Erde 75, 155–183.
Mittlefehldt, D.W., Herrin, J.S., Quinn, J.E., Mertzman, S.A., Cartwright, J.A., Mertzman, K.R., Peng, Z.X., 2013. Composition and petrology of HED polymict breccias: the regolith of (4) vesta. Meteorit. Planet. Sci. 48, 2105–2134.
Murchie, S.L., Klima, R.L., Denevi, B.W., Ernst, C.M., Keller, M.R., Domingue, D.L., Blewett, D.T., Chabot, N.L., Hash, C., Malaret, E., Izenberg, N.R., Vilas, F., Nittler, L.R., Head, J.W., 2015. Orbital multispectral mapping of mercury using the MESSENGER mercury dual imaging System: evidence for the origins of plains units and low-reflectance material. Icarus 254, 287–305.
Murray, B.C., 1975. The mariner 10 pictures of Mercury: an overview. J. Geophys. Res. 80, 2342–2344.
Namur, O., Collinet, M., Charlier, B., Grove, T.L., Holtz, F., McCammon, C., 2016. Melting processes and mantle sources of surface lavas on mercury. Earth Planet. Sci. Lett. 439.
Nekvasil, H., McCubbin, F.M., Harrington, A., Elardo, S., Lindsley, D.H., 2009. Linking the chassigny meteorite and the martian surface rock Backstay: insights into igneous crustal differentiation processes on mars. Meteorit. Planet. Sci. 44, 853–869.
Nekvasil, H., Filiberto, J., McCubbin, F.M., Lindsley, D.H., 2007. Alkalic parental magmas for the chassignites. Meteorit. Planet. Sci. 42, 979–992.
Ness, N.F., Behannon, K.W., Lepping, R.P., Whang, Y.C., 1975. The magnetic field of mercury. J. Geophys. Res. 80, 2708–2716.
Ness, N.F., Behannon, K.W., Lepping, R.P., Whang, Y.C., Schatten, K.H., 1974. Magnetic field observations near Mercury: preliminary results from mariner 10. Science 185, 151–160.
Nittler, L.R., Starr, R.D., Weider, S.Z., McCoy, T.J., Boynton, W.V., Ebel, D.S., Ernst, C.M., Evans, L.G., Goldsten, J.O., Hamara, D.K., Lawrence, D.J., McNutt, R.L., Schlemm, C.E., Solomon, S.C., Sprague, A.L., 2011. The major-element composition of mercury's surface from MESSENGER X-ray spectrometry. Science 333, 1847–1850.
Oberst, J., Preusker, F., Phillips, R.J., Watters, T.R., Head, J.W., Zuber, M.T., Solomon, S.C., 2010. The morphology of mercury's caloris basin as seen in MESSENGER stereo topographic models. Icarus 209, 230–238.
Ostrach, L.R., Robinson, M.S., Whitten, J.L., Fassett, C.I., Strom, R.G., Head, J.W., Solomon, S.C., 2015. Extent, age, and resurfacing history of the northern smooth plains on mercury from MESSENGER observations. Icarus 250, 602–622.
Peplowski, P.N., Evans, L.G., Hauck, S.A., McCoy, T.J., Boynton, W.V., Gillis-Davis, J.J., Ebel, D.S., Goldsten, J.O., Hamara, D.K., Lawrence, D.J., McNutt, R.L., Nittler, L.R., Solomon, S.C., Rhodes, E.A., Sprague, A.L., Starr, R.D., Stockstill-Cahill, K.R., 2011. Radioactive elements on mercury's surface from MESSENGER: implications for the planet's formation and evolution. Science 333, 1850–1852.
Peplowski, P.N., Evans, L.G., Stockstill-Cahill, K.R., Lawrence, D.J., Goldsten, J.O., McCoy, T.J., Nittler, L.R., Solomon, S.C., Sprague, A.L., Starr, R.D., Weider, S.Z., 2014. Enhanced sodium abundance in mercury's north polar region revealed by the MESSENGER gamma-ray spectrometer. Icarus 228, 86–95.
Peplowski, P.N., Klima, R.L., Lawrence, D.J., Ernst, C.M., Denevi, B.W., Frank, E.A., Goldsten, J.O., Murchie, S.L., Nittler, L.R., Solomon, S.C., 2016. Remote sensing evidence for an ancient carbon-bearing crust on mercury. Nat. Geosci 9, 273–276.
Peplowski, P.N., Lawrence, D.J., Evans, L.G., Klima, R.L., Blewett, D.T., Goldsten, J.O., Murchie, S.L., McCoy, T.J., Nittler, L.R., Solomon, S.C., Starr, R.D., Weider, S.Z., 2015a. Constraints on the abundance of carbon in near-surface materials on Mercury: results from the MESSENGER gamma-ray spectrometer. Planet. Space Sci 108, 98–107.
Peplowski, P.N., Lawrence, D.J., Feldman, W.C., Goldsten, J.O., Bazell, D., Evans, L.G., Head, J.W., Nittler, L.R., Solomon, S.C., Weider, S.Z., 2015b. Geochemical terranes of mercury's northern hemisphere as revealed by MESSENGER neutron measurements. Icarus 253, 346–363.
Peplowski, P.N., Lawrence, D.J., Rhodes, E.A., Sprague, A.L., McCoy, T.J., Denevi, B.W., Evans, L.G., Head, J.W., Nittler, L.R., Solomon, S.C., Stockstill-Cahill, K.R., Weider, S.Z., 2012a. Variations in the abundances of potassium and thorium on the surface of Mercury: results from the MESSENGER gamma-ray spectrometer. J. Geophys. Res. - Planets 117.
Peplowski, P.N., Rhodes, E.A., Hamara, D.K., Lawrence, D.J., Evans, L.G., Nittler, L.R., Solomon, S.C., 2012b. Aluminum abundance on the surface of Mercury: applications of a new background-reduction technique for the analysis of gamma-ray spectroscopy data. J. Geophys. Res. 117, E00L10.
Polat, A., Hofmann, A.W., Rosing, M.T., 2002. Boninite-like volcanic rocks in the 3.7-3.8 ga isua greenstone belt, west Greenland: geochemical evidence for intra-oceanic subduction zone processes in the early earth. Chem Geol 184.
Riner, M.A., Lucey, P.G., Desch, S.J., McCubbin, F.M., 2009. Nature of opaque components on Mercury: insights into a mercurian magma ocean. Geophys. Res. Lett. 36.
Riner, M.A., McCubbin, F.M., Lucey, P.G., Talyor, G.J., Gillis-Davis, J.J., 2010. Mercury surface composition: integrating petrologic modeling and remote sensing data to place constraints on FeO abundance. Icarus 209, 301–313.
Riner, M.A., Lucey, P.G., McCubbin, F.M., Taylor, G.J., 2011. Constraints on mercury's surface composition from MESSENGER neutron spectrometer data. Earth Planet. Sci. Lett. 308, 107–114.
Robinson, M.S., Lucey, P.G., 1997. Recalibrated Mariner 10 color mosaics: Implications for Mercurian volcanism. Science 275, 197–200.
Robinson, M.S., Murchie, S.L., Blewett, D.T., Domingue, D.L., Hawkins, S.E., Head, J.W., Holsclaw, G.M., McClintock, W.E., McCoy, T.J., McNutt, R.L., Prockter, L.M., Solomon, S.C., Watters, T.R., 2008. Reflectance and color variations on Mercury: Regolith processes and compositional heterogeneity. Science 321, 66–69.
Rudnick, R.L., Gao, S., 2003. Composition of the continental crust. Treatise on Geochem. 3, 1–64.
Santos, A.R., Agee, C.B., McCubbin, F.M., Shearer, C.K., Burger, P.V., Tartese, R., Anand, M., 2015. Petrology of igneous clasts in northwest Africa 7034: implications for the petrologic diversity of the martian crust. Geochim Cosmochim Acta 157, 56–85.
Sautter, V., Toplis, M.J., Beck, P., Mangold, N., Wiens, R., Pinet, P., Cousin, A., Maurice, S., LeDeit, L., Hewins, R., Gasnault, O., Quantin, C., Forni, O., Newsom, H., Meslin, P.-Y., Wray, J., Bridges, N., Payré, V., Rapin, W., Le Mouélic, S., 2016. Magmatic complexity on early mars as seen through a combination of orbital, in-situ and meteorite data. Lithos 254–255, 36–52.
Schmidt, M.E., Campbell, J.L., Gellert, R., Perrett, G.M., Treiman, A.H., Blaney, D.L., Olilla, A., Calef, F.J., Edgar, L., Elliott, B.E., Grotzinger, J., Hurowitz, J., King, P.L., Minitti, M.E., Sautter, V., Stack, K., Berger, J.A., Bridges, J.C., Ehlmann, B.L., Forni, O., Leshin, L.A., Lewis, K.W., McLennan, S.M., Ming, D.W., Newsom, H., Pradler, I., Squyres, S.W., Stolper, E.M., Thompson, L., VanBommel, S., Wiens, R.C., 2014. Geochemical diversity in first rocks examined by the curiosity rover in gale Crater: evidence for and significance of an alkali and volatile-rich igneous source. J. Geophys. Res.-Planets 119, 64–81.
Seddio, S.M., Jolliff, B.L., Korotev, R.L., Zeigler, R.A., 2013. Petrology and geochemistry of lunar granite 12032,366-19 and implications for lunar granite petrogenesis. Am. Mineral 98, 1697–1713.
Sehlke, A., Whittington, A.G., 2015. Rheology of lava flows on Mercury: an analog experimental study. J. Geophys. Res.-Planets 120, 1924–1955.
Sehlke, A., Whittington, A.G., Robert, B., Harris, A., Gurioli, L., Medard, E., 2014. Pahoehoe to 'a'a transition of hawaiian lavas: an experimental study. Bull. Volcanol. 76, 879.
Sharp, Z.D., McCubbin, F.M., Shearer, C.K., 2013. A hydrogen-based oxidation mechanism relevant to planetary formation. Earth Planet. Sci. Lett. 380, 88–97.
Solomon, S.C., McNutt Jr., R.L., Gold, R.E., Acuˉna, M.H., Baker, D.N., Boynton, W.V., Chapman, C.R., Cheng, A.F., Gloeckler, G., Head, J.W., Krimigis, S.M., McClintock, W.E., Murchie, S.L., Peale, S.J., Phillips, R.J., Robinson, M.S., Slavin, J.A., Smith, D.E., Strom, R.G., Trombka, J.I., Zuber, M.T., 2001. The MESSENGER mission to Mercury: scientific objectives and implementation. Planet. Space Sci. 49, 1445–1465.
Sprague, A.L., Roush, T.L., 1998. Comparison of laboratory emission spectra with mercury telescopic data. Icarus 133, 174–183.
Stockstill-Cahill, K.R., McCoy, T.J., Nittler, L.R., Weider, S.Z., Hauck II, S.A., 2012. Magnesium-rich crustal compositions on Mercury: implications for magmatism from petrologic modeling. J. Geophys. Res. 117, E00L15.
Stolper, E.M., Baker, M.B., Newcombe, M.E., Schmidt, M.E., Treiman, A.H., Cousin, A., Dyar, M.D., Fisk, M.R., Gellert, R., King, P.L., Leshin, L., Maurice, S., McLennan, S.M., Minitti, M.E., Perrett, G., Rowland, S., Sautter, V., Wiens, R.C., Team, M.S., 2013. The petrochemistry of Jake_M: a martian mugearite. Science 341.
Taylor, G.J., 2009. Ancient lunar Crust: Origin, Composition, and implications. Elements 5, 17–22.

Taylor, G.J., Scott, E.R.D., 2004. Mercury. In: Davis, A.M. (Ed.), Treatise on Geochemistry: Meteorites, Comets and Planets. Elsevier, Amsterdam, The Netherlands, pp. 477–485.
Taylor, S.R., McLennan, S.M., 2009. Planetary Crusts: Their Composition, Origin and Evolution. Cambridge University Press.
Thomas, R.J., Rothery, D.A., Conway, S.J., Anand, M., 2014. Long-lived explosive volcanism on mercury. Geophys. Res. Lett. 41, 6084–6092.
Vander Kaaden, K.E., McCubbin, F.M., 2015. Exotic crust formation on Mercury: consequences of a Shallow, feo-poor mantle. J. Geophys. Res. - Planets 120, 195–209.
Vander Kaaden, K.E., McCubbin, F.M., 2016. The origin of boninites on Mercury: an experimental study of the northern volcanic plains lavas. Geochim Cosmochim Acta 173, 246–263.
Vilas, F., 1988. Surface composition of Mercury from reflectance spetrophotometry. In: Vilas, F., Chapman, C.R., Matthews, M.S. (Eds.), Mercury. Univ of Arizona Press, Tucson, Arizona, pp. 59–76.
Wadhwa, M., 2008. Redox conditions on small bodies, the Moon, and mars. Oxyg. Solar Syst. 68, 493–510.
Warren, P.H., Kallemeyn, G.W., Huber, H., Ulff-Møller, F., Choe, W., 2009. Siderophile and other geochemical constraints on mixing relationships among HED-meteoritic breccias. Geochim Cosmochim Acta 73, 5918–5943.
Weider, S.Z., Nittler, L.R., Murchie, S.L., Peplowski, P.N., McCoy, T.J., Kerber, L., Klimczak, C., Ernst, C.M., Goudge, T.A., Starr, R.D., Izenberg, N.R., Klima, R.L., Solomon, S.C., 2016. Evidence from MESSENGER for sulfur- and carbon-driven explosive volcanism on Mercury. Geophys. Res. Lett. 43 (8), 3653–3661.
Weider, S.Z., Nittler, L.R., Starr, R.D., Crapster-Pregont, E.J., Peplowski, P.N., Denevi, B.W., Head, J.W., Byrne, P.K., Hauck II, S.A., Ebel, D.S., Solomon, S.C., 2015. Evidence for geochemical terranes on Mercury: Global mapping of major elements with MESSENGER's X-Ray Spectrometer. Earth Planet. Sci. Lett 416, 109–120.
Weider, S.Z., Nittler, L.R., Starr, R.D., McCoy, T.J., Solomon, S.C., 2014. Variations in the abundance of iron on mercury's surface from MESSENGER X-Ray spectrometer observations. Icarus 235, 170–186.
Weider, S.Z., Nittler, L.R., Starr, R.D., McCoy, T.J., Stockstill-Cahill, K.R., Byrne, P.K., Denevi, B.W., Head, J.W., Solomon, S.C., 2012. Chemical heterogeneity on mercury's surface revealed by the MESSENGER X-Ray spectrometer. J. Geophys. Res. - Planets 117.
Wilson, A.H., 2003. A new class of silica enriched, highly depleted komatiites in the southern kaapvaal Craton, south africa. Precambrian Res. 127, 125–141.
Zolotov, M.Y., Sprague, A.L., Hauck, S.A., Nittler, L.R., Solomon, S.C., Weider, S.Z., 2013. The redox state, FeO content, and origin of sulfur-rich magmas on mercury. J. Geophys. Res.-Planets 118.